# In situ study of the carbon gasification reaction of highly oriented pyrolytic graphite promoted by cobalt oxides and the novel nanostructures appeared after reaction.

C. Morales[1], D. Díaz-Fernández[1], P. Prieto[1], YH Lu[2], H. Kersell[2], A. del Campo[3], C. Escudero[4], V. Pérez-Dieste[4], P. Ashby[5], J. Méndez[6], L. Soriano[1*]

[1] *Departamento de Física Aplicada and Instituto de Ciencia de Materiales Nicolás Cabrera, Universidad Autónoma de Madrid, Francisco Tomás y Valiente 7, E-28049 Madrid, Spain.*

[2] *Materials Sciences Division and Chemical Sciences Division, Lawrence Berkeley National Laboratory, 1 Cyclotron Road, Berkeley, CA 94720, USA.*

[3] *Instituto de Cerámica y Vidrio, ICV-CSIC, C/Kelsen, 5, E-28049 Madrid, Spain*

[4] *ALBA Synchrotron Light Source, Carrer de la Llum 2-26, E-08290 Cerdanyola del Vallès, Spain*

[5] *The Molecular Foundry, Lawrence Berkeley National Laboratory, 1 Cyclotron Road, Berkeley, CA 94720, USA*

[6] *Instituto de Ciencia de Materiales de Madrid, ICMM-CSIC, Sor Juana Inés de la Cruz, 3, E-28049 Madrid, Spain*

## A B S T R A C T

Cobalt interaction and its effects on carbon-based systems at the nanoscale have recently attracted much attention in different fields, such as catalysis of carbon nanotubes or graphene and graphite nano-patterning taking advantage of its ferromagnetic behavior. Experiments performed in our laboratories show how the re-oxidation process of two equivalent monolayers of CoO deposited on highly oriented pyrolytic graphite at 400 °C leads to the formation of nanochannels at lower temperature than using other methods. Here we present the *in-situ* characterization of the carbon gasification reaction that drives this process by means of near ambient pressure X-ray photoelectron spectroscopy performed at the ALBA synchrotron facility. The reason why this reaction takes place at such low temperature compared to other methods is due to the weakening of the carbon σ bonds by the initial CoO wetting layer formed at the early stages of growth on the graphite surface. Besides nanochannels, *ex-situ* atomic force microscopy measurements also show the appearance of two more kinds of nanostructures: nano-strips and nano-

* Corresponding author: E-mail: l.soriano@aum.es (Leonardo Soriano)

rings. The appearance of these nanostructures reveals the impressive modification of the surface after the re-oxidation process mediated by the cobalt oxide.

## 1. Introduction

Nowadays cobalt is an essential catalytic element used in a wide variety of industrial processes, highlighting Fischer−Tropsch synthesis. Although cobalt behavior at macroscopic scale has been thoroughly characterized in the last decades, atomic scale details of the interactions between cobalt and different substrates and reactants remain under discussion [1]. In particular, its interaction and effects on carbon-based systems at the nanoscale have recently attracted much attention. For instance, it is well known that metallic cobalt catalyzes the formation of carbon nanotubes (CNTs) [2]. On the other hand, since the discovery of graphene, the fabrication of nanostructures by patterning on graphene and graphite surfaces has become a hot research topic due to multiple technological applications in a wide range of fields such as electronics [3], sensors [4], light processing [5] or energy storage [6], among others. In this regard, different works have been done also with Ni, Ag, Co and Fe nanoparticles [7,8,9,10]. Moreover, graphene and graphite nano-chanelling by Co nanoparticles at about 550 ºC in air can be controlled by taking advantage of their ferromagnetic behavior [11]. However, the atomic scale mechanisms behind these processes are still mostly unknown, which hinders the control and applications of these novel nanostructures.

Previous experiments presented by us showed a novel method of nano-patterning in highly oriented pyrolytic graphite (HOPG) via carbon gasification under oxygen atmosphere at 400 °C, starting with cobalt oxide (CoO) as catalyst material instead of typical metallic cobalt nanoparticles [12]. Compared to similar studies using metallic nanoparticles (Ni, Ag, Co and Fe), our channeling method significantly reduces the

reaction temperature, leading to an improvement of the reaction efficiency. A qualitative model of the process based on the initial weakening of the graphite σ bonds was suggested as explanation, although no direct evidence of the graphite lattice modification by the CoO during the reaction could be shown. Compared to Co nanoparticles, initial CoO deposition tends to create defects and oxidize the uppermost layers of graphite, which may facilitate the subsequent carbon gasification reaction. A complete characterization of the early stages of growth of CoO on HOPG and the initial interaction between both materials at room temperature can be found elsewhere [13,14]. However, the inability to follow the reaction process *in-situ* by conventional X-Ray photoelectron spectroscopy (XPS) has hindered its description and the comprehension of the role of each actor during the intermediate steps of heating and oxygen exposure.

As a consequence of the same carbon gasification reaction, through atomic force (AFM) and Kelvin probe force (KPFM) microscopies characterization we report the appearance of two new types of nanostructures: nano-strips and nano-rings. As it has been previously reported in the literature, both carbon and cobalt based systems, have the ability to promote and lead to novel and exotic nanostructures. For example, similar features have been found at the early stages of growth of carbon nanotubes (CNTs) [15], metal nano-rings promoted by carbon-based surfaces [16], Co superparamagnetic nano-rings [17] or $Co_3O_4$ nano-rings [18]. Due to their low dimensionality, all these structures have attracted much attention because of their novel properties compared to bulk materials. Furthermore, the interaction between different types of liquid solutions with solid surfaces have also attracted attention in the last decades due to its importance on many physical, chemical and industrial processes. In this way, self-assemblies of organic and inorganic molecules forming nano-strips on graphitic samples have been the focus of a great number of publications in the last decades [19, 20, 21].

In this work, we present *in-situ* near ambient pressure X-Ray photoelectron spectroscopy (NAP-XPS) measurements performed at the ALBA synchrotron facility. We first describe the effects of CoO deposition and further oxygen exposure on HOPG. After that, we focus on the characterization of the kinetics and transient chemical states of the carbon and Co atoms during the complete carbon gasification process, which implies initial reduction of the CoO to metallic Co nanoparticles and subsequent oxidation due to oxygen exposure, leading to the carbon gasification reaction and a very defective HOPG surface. Finally, we discuss *ex-situ* AFM/KPFM measurements of the re-oxidized surface, focusing on the appearance of new novel nanostructures such as nano-rings and nano-strips.

## 2. Experimental details

The HOPG substrates (ZYB grade, supplied by Bruker) were cleaved using scotch tape, and then cleaned by annealing at 400 °C under ultra-high vacuum conditions (below $2x10^{-8}$ mbar). The experiments started with the deposition of ~2 equivalent monolayers (Eq-ML) of CoO Cobalt oxide by reactive thermal evaporation of metallic cobalt rods (HMW Hauner, 99.99+ % purity) under oxygen atmosphere at $2\times10^{-5}$ mbar. The substrates were maintained at room temperature during the evaporation process. The growth was carried out in two different vacuum chambers: the NAPP endstation at the ALBA synchrotron's BL24-CIRCE beamline and the deposition chamber attached to a XPS spectrometer in our laboratory in Madrid. In both cases, the evaporation rate was maintained constant and low. More details describing the quantification of the growth rate can be found elsewhere [22].

*In-situ* NAP-XPS measurements were performed at the NAPP endstation of the ALBA synchrotron's BL24-CIRCE beamline [23], equipped with a PHOIBOS 150 NAP

analyzer. An overall ΔE of 0.2 eV was estimated at a photon energy of 500 eV, pass energy of 10 eV and 20 μm exit slit aperture. The XPS binding energy was corrected using the clean HOPG C 1s peak (pure $sp^2$ contribution) at 284.3 eV [24]. For these energy correction purposes, this region was measured for all photon energies and under all environmental conditions. The spectra have been fitted using the XPS Peak software, version 4.1. The fitting curves were modelled by a symmetrical Gaussian-Lorentzian sum, fixing for the C 1s and O 1s components same values, respectively. The asymmetrical graphitic $sp^2$ contribution was fitted by adding a tail modifier to the Gaussian-Lorentzian shapes. Measurements were performed at different photon energies in order to guarantee same photoelectrons kinetic energies of 220 and 700 eV for different regions. In addition, further photon energies were used for acquiring depth probe data. The inelastic electron mean free path (IMFP) for different energies trough the HOPG and CoO matrix were calculated by using the Tanuma, Powell, and Penn formula IMFP-TPP2M [25]. The XAS spectra were collected in the total electron yield mode by measuring the drain current from the sample, and normalized to the $I_0$ current measured from a gold reference sample. Some samples grown at our laboratory following the same method were used for *ex-situ* confocal Raman spectroscopy measurements and AFM imaging. Raman spectra were taken with a confocal Raman microscope (Witec ALPHA 300RA), with laser excitation at 532 nm and a 100x objective lens (NA = 0.9). The incident laser power was 1 mW. The optical diffraction resolution was limited to about 200 nm laterally and 500 nm vertically while Raman spectral resolution of the system was down to 0.02 $cm^{-1}$. The images were processed and analyzed with the software WiTec Project Plus 2.08. AFM images were obtained with a Nanotec AFM microscope in non-contact dynamic (tapping) mode. The images were processed and analyzed with the WSxM software [26]. *Ex-situ* KPFM measurements were performed at the Molecular Foundry facility (LBNL,

Berkeley, USA), in a single-pass frequency modulation mode using Cypher ES (Asylum Research) and a HF2LI lock-in amplifier (Zurich Instrument) at room temperature and nitrogen atmosphere [27,28].

## 3. Results and discussion

### *3.1. Carbon gasification reaction*

#### *3.1.1. The role of cobalt oxide in the creation of defects on HOPG*

It is well known that oxygen molecules do not absorb on HOPG surfaces at room temperature [29]. Nevertheless, deposition of CoO has been found to promote the creation of defects at the graphite surface and, afterwards, the oxidation of graphite, as reported by our group [14]. The C 1s XPS spectra depicted in Figure 1a show the effects of 2 Eq-ML of CoO on HOPG after being exposed to different $O_2$ pressures during one hour at room temperature. For low pressures ($10^{-3}$ mbar) (see inset in Fig. 1a), a very weak

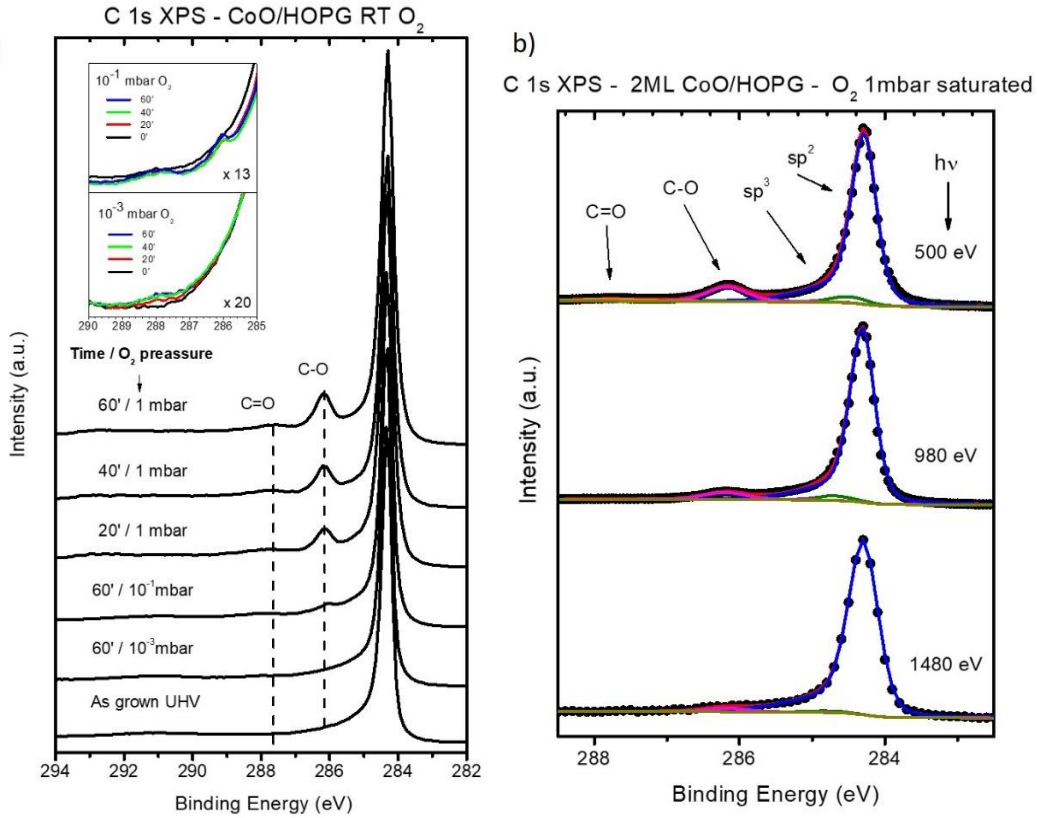

Figure 1: a) C 1s NAP-XPS measurements of 2 ML CoO/HOPG sample exposed to different $O_2$ pressures during 1 hour. The spectra taken for each pressure at different times during this exposure are labeled accordingly. The inset shows a zoom of the temporal evolution of the samples exposed to $10^{-3}$ and $10^{-1}$ mbar, respectively; b) C 1s NAP-XPS measurements with three different photon energies at 1 mbar of $O_2$.

contribution appears at 288.0 eV, corresponding to C=O bonds. After one hour of exposure at $10^{-1}$ mbar, a second component at 286.0 eV appears which belongs to C-O bonds. At higher pressures (1 mbar), this second contribution dominates and becomes clearly visible. Figure 1b shows the C 1s spectra at the saturated state of 1 mbar with different photon excitation energies, i.e. for different electron inelastic mean free paths (IMPFs) of the photoelectrons through the CoO matrix. The IMFPs values are 9.5 Å, 20.4 Å and 30.8 Å for photon energies of 500 eV, 980 eV and 1480 eV, respectively. It is shown that oxidation is mainly produced on the topmost layers of the substrate, at the CoO/HOPG interface. Therefore, the oxidation of graphite after deposition of cobalt oxide has been clearly evidenced. The oxidation is ruled by the percentage of the initially covered HOPG surface after CoO deposition. In this regard, the CoO growth on HOPG follows a Stranski-Krastanov growth mode, i.e. formation of a wetting layer followed by the creation of islands [13]. For coverages below 1 Eq-ML, CoO starts accumulating on the HOPG steps, and simultaneously, a CoO wetting layer of one-unit cell starts covering the HOPG terraces, reaching a 30% of the total surface for coverages around 2 Eq-ML. Therefore, the CoO wetting layer has an important role in the oxidation of HOPG, as it maximizes the interface between CoO and graphite thus leading to the injection of oxygen into the HOPG substrate. More details on the electronic structure of the CoO/HOPG wetting layer can be found elsewhere [14].

On the other hand, the as grown CoO layer is also altered by the presence of oxygen during the reaction. Figure SI 1 of Supporting Information shows the Co $L_{2,3}$ edge XAS spectra of both the as grown CoO and after oxygen exposure at 1 mbar. The reported

changes correspond to a further oxidation of the deposit from CoO to $Co_3O_4$ [12]. The anisotropy observed at both beam polarizations at the multiple structure for the initial deposit is related to a distortion of the Co coordination octahedron, which is produced by a strong interaction between the grown cobalt oxide and the HOPG substrate, especially at the wetting layer [13]. This assumption is also supported by previously reported AFM images of this wetting layer [13,14], as they show how it distributed itself along the crystallographic directions of the substrate. However, after 1 hour of $O_2$ exposure at 1 mbar (Figure 2c), this anisotropy has disappeared, which may indicate that the spinel $Co_3O_4$ layer has grown homogeneously.

*3.1.2. Reduction and re-oxidation process*

The re-oxidation process that give rise to the carbon gasification reaction with the formation of nanochannels takes place when heating the CoO/HOPG sample at 400 °C in ultra-high-vacuum (UHV) conditions, followed by oxygen exposure at this temperature [12]. In the present study, exposures during 1 hour to $10^{-3}$ mbar and 1 mbar $O_2$ pressures were used. The initial annealing process in UHV conditions induces the reduction of the cobalt oxide into metallic nanoparticles. Fig 2a shows the gradual reduction of $Co_3O_4$ to CoO and then to metallic cobalt. Thus, recalling Figure SI 1, the first remarkable fact is that the oxidation and reduction processes of the cobalt oxide layer are reversible, in agreement with previous works [30]. After a slow heating ramp, the complete reduction of cobalt is achieved after two hours heating (see top red spectrum). This is noticeably longer than reducing from as grown 2 Eq ML of CoO on HOPG [12], as corresponds to two reduction processes: $Co_3O_4 \rightarrow CoO \rightarrow$ metallic Co. Figure 2.b shows the Co $L_{2,3}$ XAS spectra for both polarizations once the reduction is completed at 415 °C. The spectra

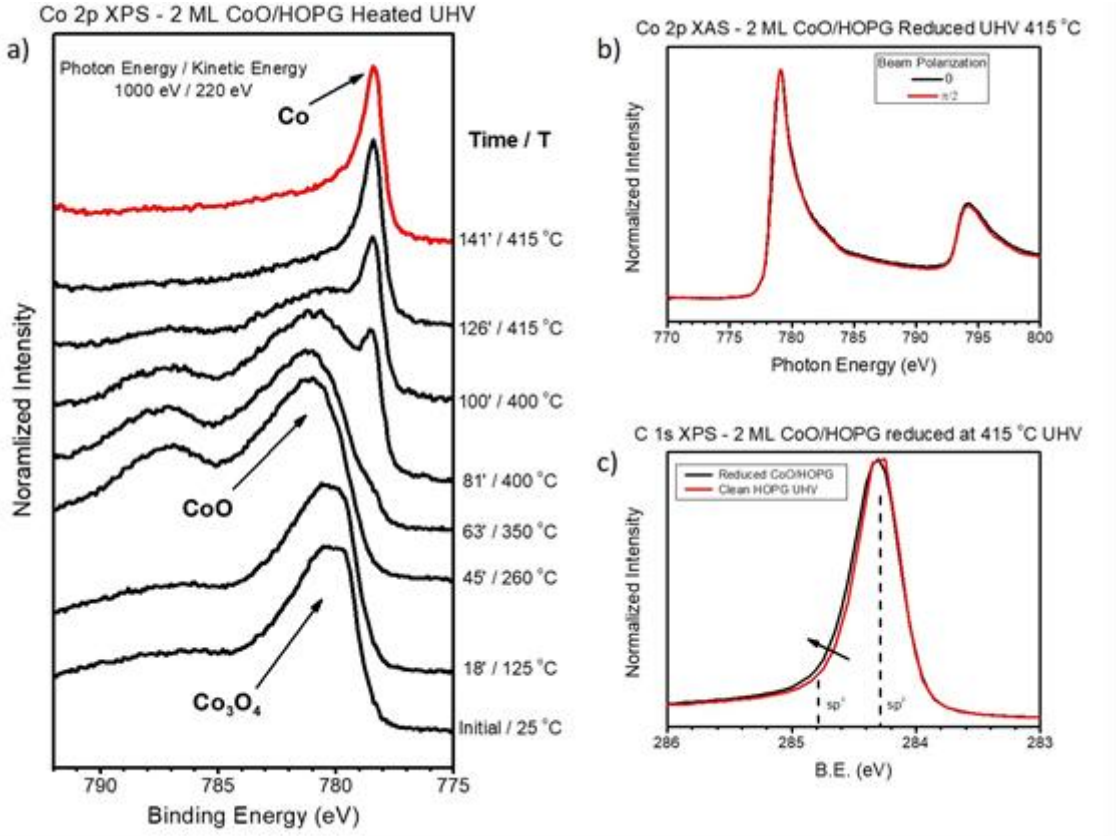


Figure 2: a) Co 2p NAP-XPS measurements as a function of time of 2 ML CoO/HOPG heated to 415°C at UHV conditions; b) Co L2,3 edge XAS measurements of 2 ML CoO/HOPG sample after reduction at 415oC in UHV conditions at two beam polarizations: 0 and π/2. c) C 1s XPS measurement of clean and reduced HOPG.

match that for metallic Co published elsewhere [12]. The initial anisotropy between both polarizations disappears, suggesting the extinction of the initial morphology in a clustering process to form new metallic Co nanoparticles. It is even more interesting to remark the changes observed on the substrate. Figure 2 c shows the C 1s XPS spectra for clean HOPG and after the reduction process of the CoO layer at 415 $^{o}$C in UHV conditions. Although the C-O and C=O contributions at ~286.0 and ~288.0 eV disappear, the main $sp^2$ hybridization peak at 284.3 eV widens at higher binding energies, indicating the $sp^3$ defects existence (~284.8 eV) [31,32].Therefore, the heating process removes the oxygen from the graphite and reduces the cobalt oxide to metallic Co, but meanwhile the graphite lattice is perturbed, presenting defects that translate in a different coordination

of the carbon atoms. The increment of the D/G Raman ratio shown in Figure 4 at this step also confirms the changes on the graphite substrate. Precisely, these defects support the hypothesis of the weakening of the σ bonds of graphite due to the interaction with cobalt oxide, which acts as an "oxygen pump" for the graphite lattice [14].

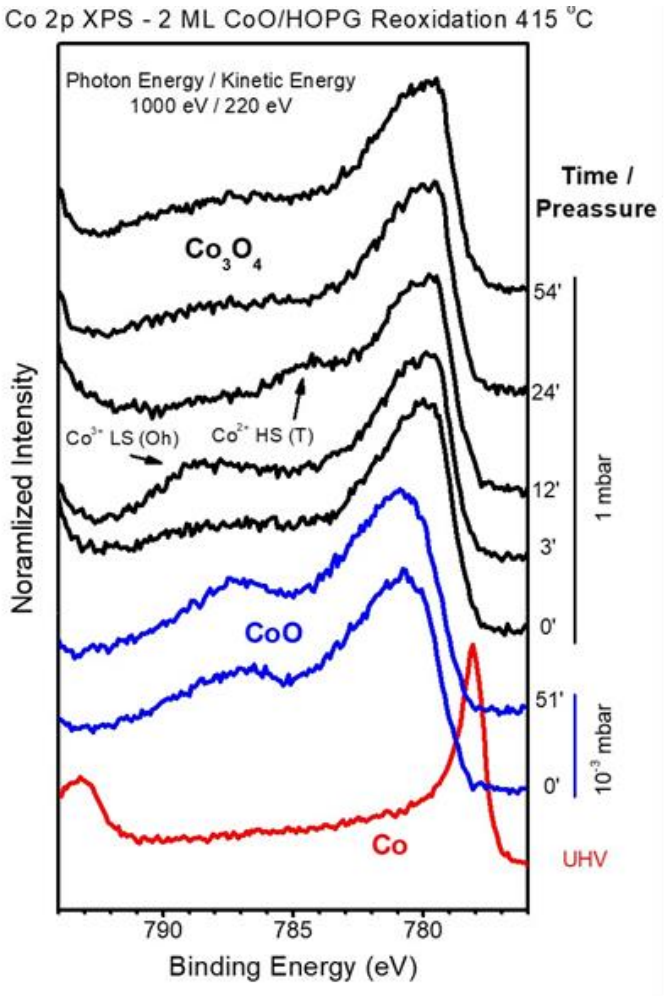


Figure 3: Co 2p NAP-XPS measurements as a function of $O_2$ pressure and time of 2 ML CoO/HOPG at 415°C

Once the temperature remains constant at about 415 ºC, exposure to oxygen produces an acceleration of the reaction kinetics. Changes of the oxidation state of cobalt are instantaneous (the first NAP-XPS spectrum for each pressure is completed just one minute after the oxygen valve is open). As shown in Figure 3, for $10^{-3}$ mbar of $O_2$ the metallic Cobalt (red) is immediately re-oxidized to CoO (blue) and remains unchanged

for further oxidation at this oxygen pressure. However, as the pressure increases to 1 mbar, the initial spectrum changes again to the characteristic shape of spinel cobalt oxide (black). As shown in Figure 3, the evolution of the Co $2p_{3/2}$ XPS spectra results rather complex, showing a variation of the relative intensity of the two characteristic satellites during the first ~20 minutes. The lattice structure of spinel $Co_3O_4$ consists of one $Co^{2+}$ cation tetrahedrally coordinated with high spin configuration ($Co^{2+}$ HS (T)) and two $Co^{3+}$ cations octahedrally coordinated with low spin configuration ($Co^{3+}$ LS ($O_h$)). Cluster model calculations [33] for Co 2p XPS spectrum (see Figure SI 2 of Supporting Information) show that the satellite corresponding to $Co^{2+}$ HS (T) is situated at ~5.5 eV above the main peak, whereas the satellite corresponding to $Co^{3+}$ LS ($O_h$) is situated at ~10.0 eV apart from the main contribution. These values match with the experimental relative position of the satellites, about 6.0 eV and 9.0 eV from the main peak respectively, as shown in the spectra taken at 1 mbar in Figure 3. At this point, it may be interesting to recall the work from G. A. Sawatzky *et. al*. [34], where it was experimentally shown on CoO, $Li_xCo_{1-x}O$ and $LiCoO_2$, the transition between $Co^{2+}$ HS (T) and $Co^{3+}$ LS ($O_h$) states as a function of the lithium doping. In fact, in the case of $LiCoO_2$, Co-O interatomic distance was strongly reduced, resulting in a ligand field strong enough to stabilize a $Co^{3+}$ low-spin ground state, which satellite dominated on the XPS Co 2p spectrum. In this way, the variation of the relative intensities of these $Co^{2+}$ HS (T) and $Co^{3+}$ LS ($O_h$) satellites seems to indicate that during the re-oxidation process at 400 ºC both, $Co^{2+}$ and $Co^{3+}$ species are being promoted alternatively for different stages of the re-oxidation process. It should be mentioned that previous Co $L_{2,3}$ XAS measurements performed after this re-oxidation process showed the formation of a mixture of spinel and CoO oxides (70/30 %) [12].

The spinel structure is a very common and well-studied system for many other

metal atoms. One of these well-known spinel systems due to its multiple applications is magnetite, the iron spinel $Fe_3O_4$. In this particular case, tetrahedral sites are occupied by $Fe^{3+}$ while octahedral sites are occupied by equal number of $Fe^{2+}$ and $Fe^{3+}$ in bulk $Fe_3O_4$. In fact, the proportion of octahedral $Fe^{2+}/Fe^{3+}$ can be modified and these atoms can be exchanged. Regarding magnetite nanoparticles, this ratio is shape [35] and size dependent [36]. In addition, plane surface termination also determines the changes in the $Fe^{2+}/Fe^{3+}$ ratio of total cations as compared to the bulk. This has been studied for the (001) terminated planes, which are mainly composed by octahedral $Fe^{2+}$ and $Fe^{3+}$ [37]. Although for $Fe_3O_4$ is relatively simple to explain the exchange between octahedral $Fe^{+2}$ and $Fe^{3+}$, its behavior can be used to inspire a hypothesis for the current cobalt spinel issue. Therefore, we propose as a possible explanation for the variation of the intensities of $Co^{2+}$ HS (T) and $Co^{3+}$ LS ($O_h$) satellites the ionic inter-exchange on the spinel structure between both states. It is known that $Co^{2+}/Co^{3+}$ ions are able to interconvert with relatively weak variations in oxidizing or reducing ambient conditions [38]. In addition, the close relationship between the rock-salt (CoO) and spinel oxygen sublattices and the ease with which cations can move between octahedral and tetrahedral sites [38], especially at the surface, suggest a possible important exchange between both states until equilibrium is reached. Note that during the present re-oxidation process a strong carbon gasification reaction driven by $CoO_x$ nanoparticles is occurring, and due to its low dimensionality, the surface is maximized over the volume. Therefore, the three conditions for $Co^{2+}/Co^{3+}$ ionic inter-exchange, i.e. strong variations in oxidizing or reducing ambient conditions and high mobility of cations throughout the surface, are fulfilled.

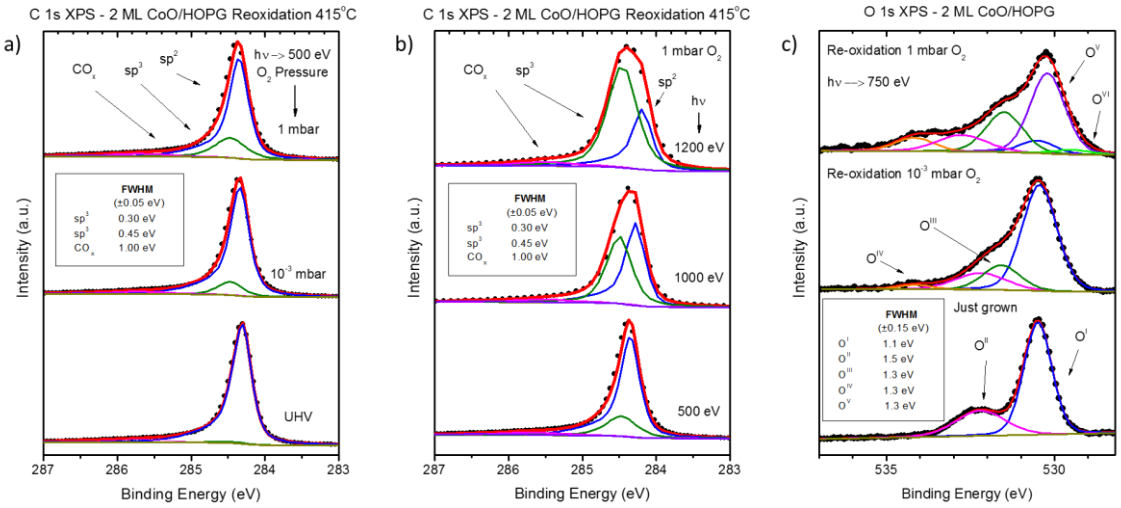


Figure 4: a) C 1s NAP-XPS measurements as a function of $O_2$ pressure of 2 ML CoO/HOPG at 415°C; b) C 1s NAP-XPS measurements with three different photon energies for 1mbar of $O_2$ at 415°C; c) O 1s NAP-XPS measurements as a function of $O_2$ pressure of 2 ML CoO/HOPG at 415°C. Bottom: as grown CoO layer.

Regarding the substrate, important changes in the C 1s XPS spectra can be reported. Figure 4a shows the evolution of the carbon species as a function of oxygen pressure. Note that the photon energy was fixed at 500 eV, so that the spectra are very sensitive to the surface (IMPF about 9.5Å). As it can be noticed, the presence of $O_2$ develops defects on the graphite lattice, labeled as $sp^3$ in Figure 4a and 4b, although the signal of C-O and C=O is much less intense than those shown in Figure 1a for the same pressures at room temperature. This can be explained by rapid desorption of the products coming from the carbon gasification reaction, so the intermediate states currently bonded to the graphite surface have very tiny signal compared to the intensity of the $sp^2$ main peak. However, important changes can be found in Figure 4b fixing $O_2$ pressure at 1 mbar and varying photon energy (IMPFs through Cobalt oxide matrix of 9.5Å, 20.8Å and 26.3Å for hν of 500 eV, 1000 eV and 1200 eV, respectively). In this case, as the probing depth is increased, the proportion of the defects peak compared to the non-perturbed graphite lattice signal dramatically increases. This tendency indicates that in this case the

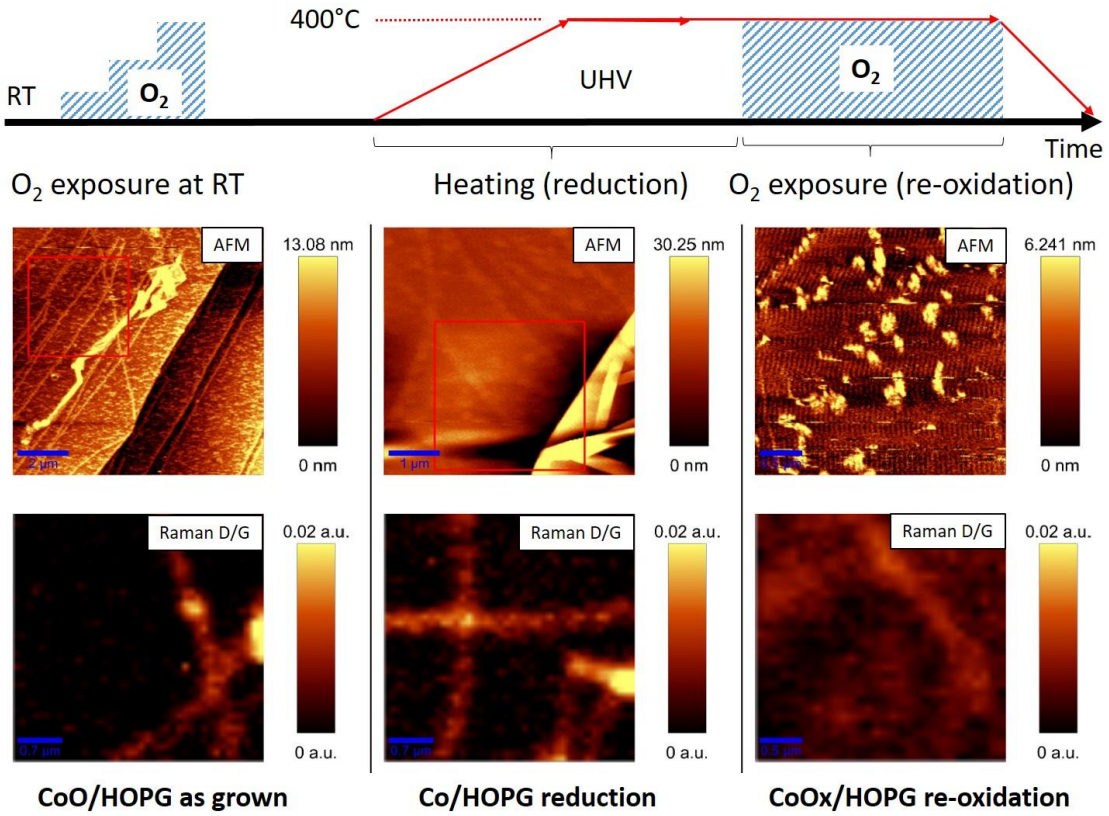


Figure 5: Top image: scheme of the experiment performed. Step 1: exposure to $O_2$ of the as grown deposit; step 2 re-oxidation process consisting of two stages: reduction at 400°C under UHV conditions and introduction of $O_2$ at that same temperature. For each of these three stages AFM (top) and Raman images of the D/G band ratio (bottom). The red squares in the AFM images are the zones mapped with Raman spectroscopy at their respective bottom images. In the case that there is not a red square, it means that the whole image has been mapped. All Raman images have been normalized to the same units for comparison purposes.

graphite defects were developed preferably under the $CoO_x$ clusters. This is in total agreement with the depth profile (XZ) micro-Raman spectroscopy measurements performed after the same re-oxidation process and shown in Figure SI 3 of Supporting Information, where the defects (D band of the graphite spectra, in green) increase all over the sample, but especially under and close to the $CoO_x$ clusters ($A_{1g}$ bands, in blue). In this manner, the increment of the $sp^3$ contribution together with the reduction of the $sp^2$ contribution for higher penetration depths does not mean that the perturbation of the graphite lattice occurs at the bulk, but at the $CoO_x$/HOPG interface. Furthermore, Raman

mappings of the D/G ratio confirm the evolution of defects on the graphite surface as a function of the stages of whole process. First, the 2 Eq-ML as grown sample shows a low but not depreciable rate of defects on the terraces (bare HOPG is almost free defective), while the reduction under UHV at 400 °C implies an increment on these defects. Thus, these measurements confirm the previous discussion regarding Figures 1b and 2c, i.e. the starting point of the carbon gasification process is characterized by a perturbed graphite lattice. Finally, the introduction of oxygen and subsequent developing of the carbon gasification reaction involves the formation of more defects on the top layers of the graphite surface.

The final products of the carbon gasification reaction (CO and $CO_2$) could not be studied directly using mass spectrometry due to the loss of the vacuum range of the spectrometer with exposures to 1 mbar. However, intermediate sates of the surface can be investigated via the O 1s XPS spectra for different $O_2$ pressures, as shown in Figure 4c. For the as grown CoO, only two contributions are observed: the main peak $O^{I}$ at 530.5 eV, which is related with the oxygen atoms in metal oxides (specifically CoO), and $O^{II}$ at 532.3 eV which is usually established to come from hydroxyl groups adsorbed at the surface of transition metal oxides [39]. As the $O_2$ pressure is increased, the spectra become more complicated since the carbon gasification reaction takes place, leading to the oxidation of CoO into $Co_3O_4$. At higher pressures, $O^{I}$ shifts to 530.2 eV ($O^{V}$, corresponding to $Co_3O_4$) and three more contributions appear and increase their relative intensity, labelled as $O^{III}$, $O^{IV}$ and $O^{VI}$. The $O^{III}$ one at 531.6 eV could be linked to oxygen singly bonded to aliphatic carbon (C-O), and may correspond to an intermediate state where the carbon ring of the graphite lattice is broken [40,41]. The $O^{IV}$ contribution is located at higher binding energy, 534.2 eV. Such high binding energies may not correspond to $CO_x$ species, but probably to different volatile silicon compounds ($SiO_x$)

from contamination of the chamber. This contamination should be taken into account since the heating of some parts of the chamber during the re-oxidation process may activate these contaminants. In fact, the XPS survey at 400°C under UHV conditions of a clean HOPG substrate shows a tiny Si 2p signal that could significantly increase under more time and aggressive reactive conditions, such as those of the re-oxidation process (see Figure SI 4). In any case, carbonyl loss structure observed in activated carbons cannot be discard [42,43]. Finally, peak $O^{VI}$ at 529.6 eV corresponds to oxygen doubly bonded to aromatic carbon (C=O) [40, 41,44]. Its lower intensity and its appearance only with high oxygen pressures may be explained as a previous stage of $O^{III}$ with a very short mean time life, as it was discussed previously for the oxidation of the HOPG by CoO at room temperature. The increase of both, graphite defects and oxygen intermediated states $O^{III}$ and $O^{VI}$ at the surface, indicates the reaction kinetics acceleration with the increase of oxygen pressure.

*3.1.3. The model of carbon gasification reaction*

Summarizing all the previous discussion, Figure 6 shows a basic model of the carbon gasification reaction. Firstly, the weakened graphite after the reduction process is characterized by the development of $sp^3$ defects, i.e. single bonded C-C and C-H. The graphitic aromatic rings were broken during the initial oxidation process of HOPG due to the presence of CoO. Although the reduction under UHV conditions eliminates the C-O and C=O species, it cannot recompose completely the broken aromatic rings. The chemical routes of HOPG being oxidized by the as deposited CoO and the carbon gasification reaction during the re-oxidation process at 400°C are quite similar. However,

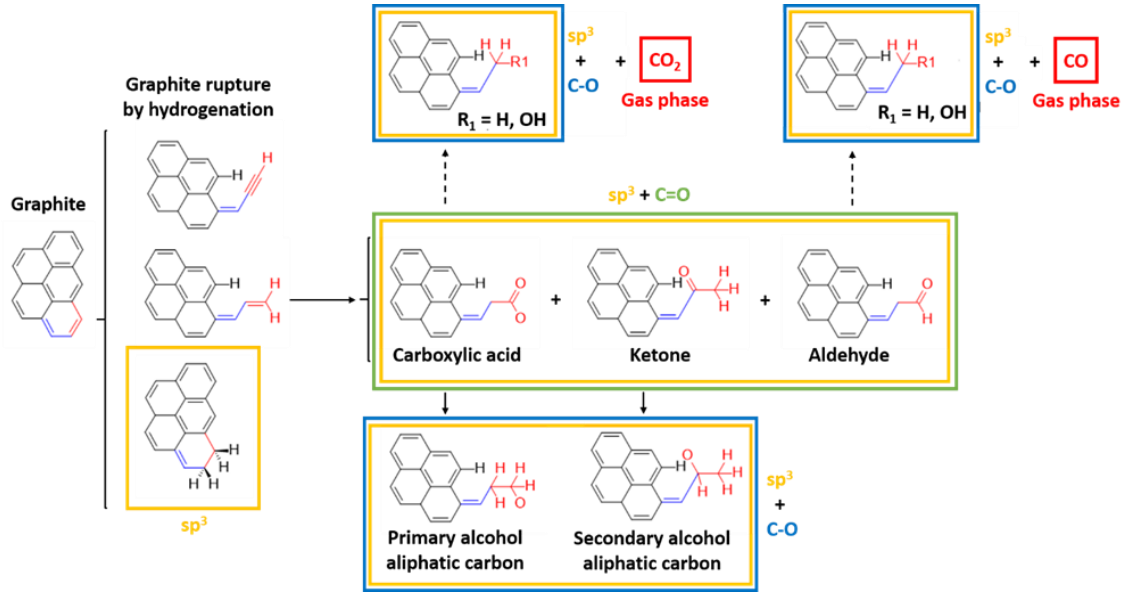


Figure 6: Basic scheme of the carbon gasification reaction induced by cobalt oxide nanoparticles on graphite via re-oxidation process.

the carbon gasification reaction is enhanced by two factors: 1) the high temperature and 2) the weakened graphite because of its broken rings from the first oxidation of the substrate. In this way, first of all the graphite rings may break up by a hydrogenation process catalyzed by the cobalt oxide which, as Figure 6 shows, can lead to three different scenarios, triple, double or single C-C bonding. From these scenes, the double bonded C=C is the one that could act as the door for the graphite oxidation. The following oxidation step would consist in the development of C=O by the formation of carboxyl, ketone and aldehyde groups. All of them are intermediate steps, with a very short mean lifetime, as it is suggested by Figures 1a and 4c, implying $sp^3$ and C=O contributions in the C 1s and O 1s spectra (yellow square corresponding to $sp^3$ hybridization and green square corresponding to C=O contribution in Figure 6). However, each of these groups can evolve in a different way. Regarding the carboxyls and ketones, the oxidation process can convert into primary and secondary alcohols, respectively, where aliphatic carbon (C-O) can be found (blue square in Figure 6 corresponding to C-O contribution). On the other hand, the carboxyl and the aldehyde can progress to $CO_2$ and CO gases, respectively (as

previously reported [12]), leading to the graphitic carbon bonded to hydrogen and/or $OH^-$ groups.

This chemical sequence can explain all the measured species from carbon and oxygen spectra as well as the evolution as a function of time and oxygen pressure, spotlighting the leading role of the initial CoO as oxidation agent of HOPG. Precisely, this initial interaction between CoO and the substrate is the key to understand how graphitic rings initially break up, weakening the graphite network and being able to induce nano-patterning at lower temperatures than those reported for metallic nanoparticles.

*3.2. Final nanostructures on the HOPG surface: an AFM-KPFM study*

*Ex-situ* AFM measurements reveal, apart from the nanometric $Co_3O_4$ islands, three different kinds of nanostructures on the graphite surface after the re-oxidation process, as shown in Figure 7 and Figure SI 5 of Supporting Information, Nanochannels have been previously described in Ref. [12], where it was shown that the nanochannels presented a width according to the size of the Co particle and a depth proportional to 1, 2 or 3 graphite planes, presenting a wide range of direct technological applications. On the other hand, nano-rings and nano-strips also appear on the HOPG surface. Unfortunately, these nanostructures are much more evasive: 1) their appearance is time dependent at ambient conditions; 2) these nanostructures tend to disappear under gentle energy flux, such as increasing temperature or electron and soft X-ray doses. This second circumstance reduces the range of chemical characterization techniques available, thus limiting the measurements to non-contact probe techniques at RT.

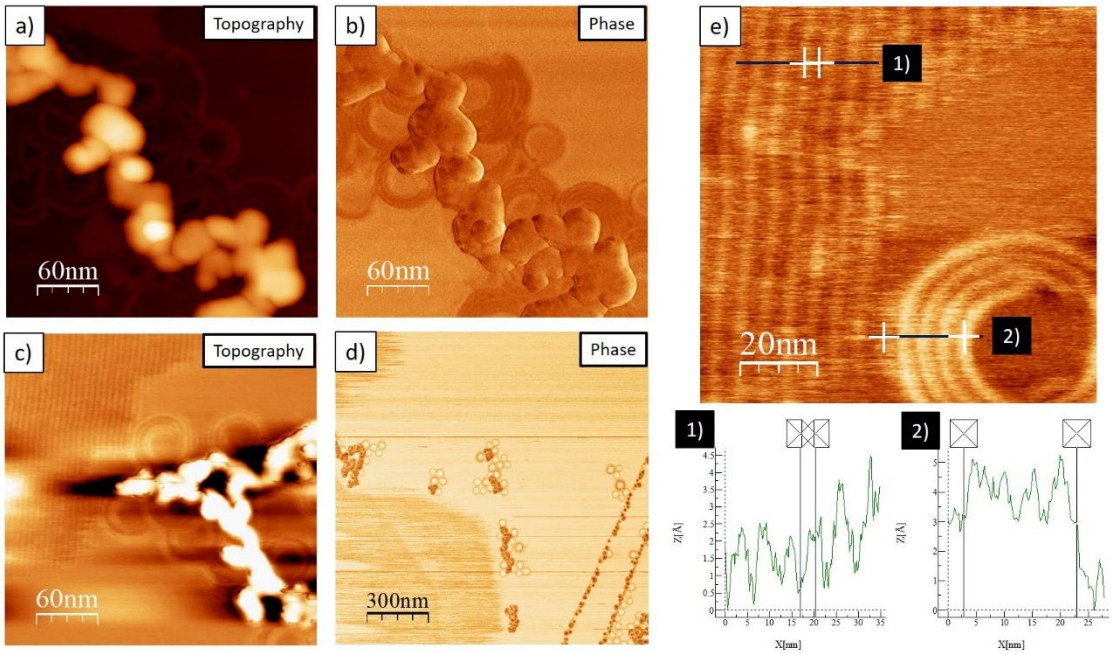


Figure 7: a) and b) topography and phase images, respectively, of 2 ML CoO/HOPG after re-oxidation process. $CoO_x$ clusters and nano-rings are shown; c) detail of nano-rings and nano-strips in topography image; d) phase image of $CoO_x$ clusters along graphite steps and terraces surrounded by nanorings. e) topography detail of nanorings and nanostrips with their corresponding profiles. Images taken with Nanotec AFM microscope at room conditions.

Topography images show a broad range of nano-rings dimensions, usually bigger when closer to $Co_3O_4$ clusters (see Figures 7, Figure SI 5 and video included in supplementary information). Nano-rings develop mainly as concentric rings in contact to the $Co_3O_4$ clusters and new nano-rings appear with time, as it can be observed in Figure SI 6 and AFM video of the Supporting Information. The movement of the nano-rings in the video is due to the tip, however, the appearance of new nano-rings with time is evident. Under the same growth conditions, the diameter of the nano-rings on different re-oxidized samples varies from 41±2 nm to 25±2 and 13±2 nm. The height of individual rings is 4-4.5 Å, whereas concentric rings (as Figure 7.e) are 1.5 Å high. This last value is the same as for the nano-strips, and could

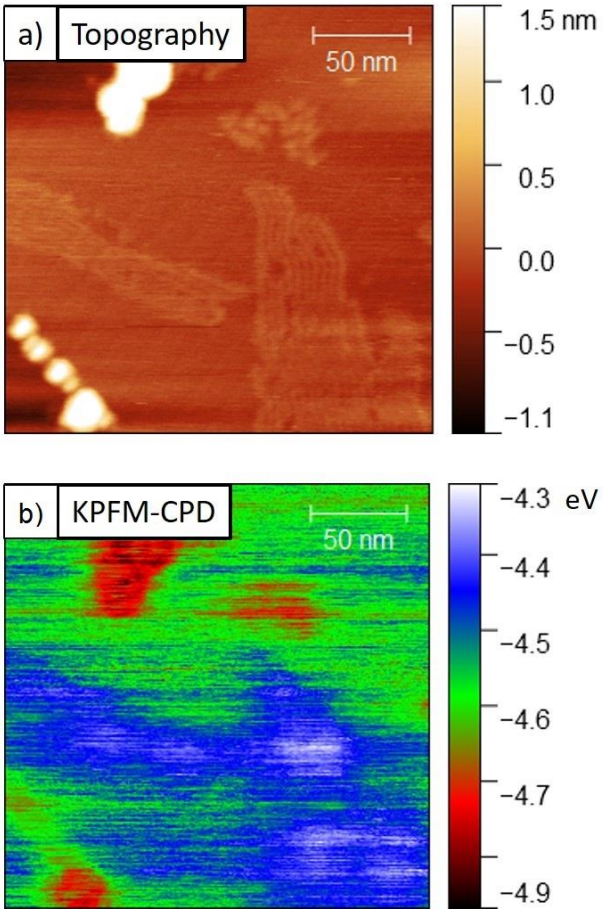


Figure 8: a) AFM topography image and b) work function map of 2 ML CoO/HOPG after re-oxidation process. A Cypher VRS microscope was used at RT and $N_2$ atmosphere.

be an overestimation due to the tip-sample convolution (tip not sharp enough to resolve the small separation between nanostructures). In particular, the periodicity of both nano-strips and concentric nano-rings is 5±0.5 nm. Finally, these periodic nano-strips are arranged along three orientations spaced 120° apart. In addition, our KPFM measurements (Figures 8.a and 8.b, topography and its corresponding work function map, respectively) show that the work function of these nano-strips is ~200 meV lower than that of bare HOPG surface. Assuming that HOPG has a work function of 4.6 eV [45,46], $Co_3O_4$ clusters show ~4.9 eV, in good agreement with other experiments [47]. Surface contamination of graphite with organic molecules after room conditions exposure leads to an increase of the work function [48], which could indicate a different origin of these

nanostructures. On the other hand, adsorption of different types of both organic [21,49] and inorganic molecules [20,50] on graphene and graphite substrates is thoroughly reported. Similar dimensions and periodicities of ~4-7 nm for this kind of nano-strips can be found for self-assembled molecule chains, which can be aligned along the armchair axis.

Although exotic structures such as CNTs [15], metal nano-rings promoted by carbon-based surfaces [16], Co superparamagnetic nano-rings [17] or $Co_3O_4$ nano-rings [18] cannot be discarded with the lack of chemical information, the observed nano-strips work function is too low for these nanostructures. Thus, it seems more plausible that these nano-rings and nano-strips are self-assembled structures of organic and/or inorganic molecules contained in the laboratory atmosphere. This could explain their time dependent appearance and their vanishing with gentle energy flow. In particular, the aforementioned weakening of the $sp^2$ structure of graphene in the surface, and especially in the surroundings of the cobalt oxide clusters after the re-oxidation process, could lead to changes on hydrophobicity and reactivity of the HOPG surface. The alteration of the surface after the re-oxidation process due to the development of defects shown in Figure 5 support this hypothesis. This could facilitate the adsorption of molecules and the curvature of the typical nano-strips where more HOPG defects can be found, turning over themselves and creating the nano-rings.

## 4. Conclusions

In summary, we have studied the carbon gasification reaction driven by CoO on HOPG by means of *in-situ* NAP-XPS. At room temperature, CoO acts as an "oxygen pump" into the graphite lattice, weakening the σ bonds of the carbon and creating defects after both the oxidation and the reduction of the graphite. This reduces the temperature at which the carbon gasification reaction occurs comparing to metallic Cobalt clusters, leading to

nano-channeling at only 400°C. During the re-oxidation process of CoO to $Co_3O_4$ clusters, an ionic inter-exchange exists in the spinel structure between $Co^{2+}$ HS (T) and $Co^{3+}$ LS ($O_h$) states until the equilibrium is reached. On the other hand, the creation of defects on the HOPG surface may facilitate the self-assembling of molecules on nano-strips along the armchair axis of graphite by the modification of its reactivity and hydrophobicity. Especially at the surroundings of $Co_3O_4$ re-oxidized clusters, the increase of expected defects might lead to the curvature of these self-assembled nano-strips into nano-rings.

**Acknowledgments**

This investigation has been funded by the MINECO of Spain through the FIS2015-67367-C2-1-P P and MAT2017-85089-C2-1-R projects and by the Comunidad de Madrid through the NANOMAGCOST-CM Ref: P2018/NMT4321 project. The experiments were performed at CIRCE/NAPP beamline at ALBA Synchrotron with the collaboration of ALBA staff. Work at the Molecular Foundry was supported by the Office of Science, Office of Basic Energy Sciences, of the U.S. Department of Energy under Contract No. DE-AC02-05CH11231. One of the authors (C.M.) thanks MECD for a FPU grant**.** Authors would like to acknowledge Dr. Concepción Sánchez-Martinez for the rich discussion of the chemical results.

**References:**

[1] S. Shetty, R.A. van Santen; **CO dissociation on Ru and Co surfaces: The initial step in the Fischer–Tropsch synthesis**; Catal. Today; 171 (2011) pp. 168–173 doi:10.1016/j.cattod.2011.04.006

[2] D. S. Bethune, C. H. Kiang, M. S. de Vries, G. Gorman, R. Savoy, J. Vazquez & R. Beyers; C**obalt-catalysed growth of carbon nanotubes with single-atomic-layer walls**; Nature; 363 (1993) pp. 605-607 doi:10.1038/363605a0

[3] F. Schwierz; **Industry-compatible graphene transistors**; Nature; 472 (2011) pp. 41–42 doi: 10.1038/472041a

[4] E. W. Hill, A. Vijayaragahvan, K. Novoselov; **Graphene Sensors**; IEEE Sensors Journal 11 (12) (2011) pp. 3161-3170 doi: 10.1109/JSEN.2011.2167608

[5] Qiaoliang Bao and Kian Ping Loh; **Graphene Photonics, Plasmonics, and Broadband Optoelectronic Devices,** ACS Nano; 6 (5) (2012) pp. 3677-3694;; doi: 10.1021/nn300989g

[6] R. Raccichini, A. Varzi, S. Passerini, B. Scrosati; **The role of graphene for electrochemical energy storage**; Nat. Mater.; 14 (2015) pp. 271-279; doi: 10.1038/nmat4170

[7] L. Ci, Z. Xu Z, L. Wang, W Gao, F Ding, K.F. Kelly, B.I. Yakobson, P.M. Ajayan; **Controlled Nanocutting of Graphene**; Nano Res; 1 (2008) pp. 116-122 doi: 10.1007/s12274-008-8020-9)

[8] N. Severin, S. Kirstein, I.M. Sokolov, J.P. Rabe; **Rapid Trench Channeling of Graphenes with Catalytic Silver Nanoparticles**; Nano Lett 9 (2009) pp. 457-461 doi: 10.1021/nl8034509

[9] S. Konishi , W. Sugimoto, Y. Murakami, Y. Takasu.; **Catalytic creation of channels in the surface layers of highly oriented pyrolytic graphite by cobalt nanoparticles**; Carbon, 44 (2006) pp. 2338-2340 doi: 10.1016/j.carbon.2006.05.003

[10] S.S. Datta, D.R. Strachan, S.M. Khamis, A.T. Johnson; **Crystallographic etching of few-layer graphene**; Nano Lett, 8 7 (2008) pp. 1912-1917 doi: 10.1021/nl080583r

[11] L. Bulut, R.H. Hurt; **A Magneto-catalytic Writing Technique for Etching Complex Channel Patterns into Graphenic Carbons**; Adv. Mater.; 22 (2010) pp. 337-341; doi: 10.1002/adma.200901932

[12] D. Díaz-Fernández, J. Méndez, A del Campo, R.J.O. Mossanek, M. Abbate, M.A. Rodríguez, G. Domínguez-Cañizares, O. Bomatí-Miguel, A Gutiérrez, L. Soriano; **Nanopatterning on highly oriented pyrolytic graphite surfaces promoted by cobalt oxides**; Carbon; 85 (2015) pp. 89-98. doi: 10.1016/j.carbon.2014.12.049

[13] D. Díaz-Fernández, J.Méndez, O. Bomatí-Miguel, F. Yubero, R.J.O. Mossanek, M. Abbate,G. Domínguez-Cañizares, A. Gutiérrez, S. Tougaard, L. Soriano; **The growth of cobalt oxides on HOPG and $SiO_2$ surfaces: A comparative study**; Surface Science; 624 (2014) pp. 145–153. doi: 10.1016/j.susc.2014.02.007

[14] C. Morales, D. Díaz-Fernández, R.J.O. Mossanek, M. Abbate, J. Méndez, V. Pérez-Dieste, C. Escudero, J. Rubio-Zuazo, P. Prieto, L. Soriano; **Controlled ultra-thin oxidation of Graphite promoted by cobalt oxides: influence of the initial 2D CoO wetting layer**; Submitted to Applied Surface Science

[15] D. Takagi, Y. Homma, H. Hibino, S. Suzuki, Y. Kobayashi; **Single-walled carbon nanotube growth from highly activated metal nanoparticles**; Nano Lett; 6 12 (2006) pp. 2642-2645. doi: 10.1021/nl061797g

[16] M. Liu, Y. Lu, W. Chen; **PdAg nano-rings supported on graphene nanosheets: highly methanol-tolerant cathode electrocatalyst for alkaline fuel cells**; Adv. Funct. Mater.; 23 (10) (2013) pp. 1289-1296. doi: 10.1002/adfm.201370050

[17] M. Marin-Almazo, D. Garcia-Gutierrez, X. Gao, J. L. Elechiguerra, V. A. Kusuma, W. M. Sampson, M. Miki-Yoshida, A. B. Dalton, R. Escudero, M. Jose-Yacaman; **Cobalt-based superparamagnetic nano-rings**; Nano Lett. 4 8 (2004) pp. 1365-1371. doi: 10.1021/nl049464b

[18] X. Liu, R. Yi, N. Zhang, R. Shi, X. Li, G. Qiu; **Cobalt hydroxide nanosheets and their thermal decomposition to cobalt oxide nano-rings**; Cheamstry Asian Jornal; 3 (2008) 732-738. doi: 10.1002/asia.200700264

[19] S. Manne, H. E. Gaub; **Molecular organization of surfactants at solid-liquid interfaces**; Science 270 (1995) pp. 1480-1482. doi: 10.1126/science.270.5241.1480

[20] Y.-H. Lu, C.-W. Yang, I.-S. Hwang,; **Atomic force microscopy study of nitrogen molecule self-assembly at the HOPG–water interface**; Appl. Surf. Sci. 304 (2014) pp. 56–64. doi: 10.1016/j.apsusc.2014.03.084

[21] P. Gallagher, M. Lee, F. Amet, P. Maksymovych, J. Wang, S. Wang, X. Lu, G. Zhang, Ke. Watanabe, T. Taniguchi, D. Goldhaber-Gordon; **Switchable friction enabled by nanoscale self-assembly on graphene**; Nat. Commun. 7 (2016) p. 10745 doi: 10.1038/ncomms10745

[22] D. Díaz-Fernández, J. Méndez, F. Yubero, G. Domínguez-Cañizares, A. Gutiérrez, L. Soriano; **Study of the early stages of growth of Co oxides on oxide substrates**; Surf. Interface Anal.; 46 (2014) pp. 975-979. doi: 10.1002/sia.5366

[23] V. Pérez-Dieste, L. Aballe, S. Ferrer, J. Nicolàs, C. Escudero, A. Milán, E. Pellegrin, **Near Ambient Pressure XPS at ALBA**. J. Phys. Conf. Ser.; 425 (7) (2013) p. 072023. doi:10.1088/1742-6596/425/7/072023

[24] M. J. Webb, P. Palmgren, P. Pal, O. Karis, H.Grennberg; **A simple method to produce almost perfect graphene on highly oriented pyrolytic graphite**; Carbon; 49 10 (2011) pp. 3242-3249. doi: 10.1016/j.carbon.2011.03.050

[25] S. Tanuma, C.J. Powell, D.R. Penn; **Proposed formula for electron inelastic mean free paths based on calculations for 31 materials;** Surf. Sci. Lett. 192 (1) (1987) pp. L849–L857; doi:10.1016/0167-2584(87)90829-2.

[26] I. Horcas, R. Fernández, J.M. Gómez Rodríguez, J. Colchero, J. Gómez Herrero, A.M. Baró; **WSXM: A software for scanning probe microscopy and a tool for nanotechnology**; Rev. Sci. Instrum. 78 (2007) p. 013705. doi: 10.1063/1.2432410

[27] Y. Zhang, D. Ziegler, M. Salmeron; **Charge Trapping States at the SiO2–Oligothiophene Monolayer Interface in Field Effect Transistors Studied by Kelvin Probe Force Microscopy**; ACS Nano 7 (2013) 8258-8265; doi: 10.1021/nn403750h

[28] Y. Zhang, O. Pluchery, L. Caillard, A.-F. Lamic-Humblot, S. Casale, Y. J. Chabal, M. Salmeron; "**Sensing the Charge State of Single Gold Nanoparticles via Work Function Measurements**"; Nano Lett.; 15 (2015) pp. 51-55. doi: 10.1021/nl503782s

[29] D.C. Sorescu, K.D. Jordan, P. Avouris; **Theoretical study of oxygen adsorption on graphite and the (8, 0) single-walled carbon nanotube**; J. Phys. Chem. B, 105 (2001) pp. 11227-11232; doi: 10.1021/jp0122979

[30] M. Oku, Y. Sato; **In-situ X-ray photoelectron spectroscopic study of the reversible phase transition between CoO and $Co_3O_4$ in oxygen of $10^{-3}$ Pa**; Appl. Surf. Sci. 55 (1992) pp. 37-41. doi: 10.1016/0169-4332(92)90378-B

[31] B. Rousseau, H. Estrade-Szwarckopf, A.-L. Thomann, P. Brault; **Stable C-atom displacements on HOPG surface under plasma low-energy argon-ion bombardment**; Applied Physics A 77 (3-4) (2003) pp 591–597. doi: 10.1007/s00339-002-1538-x.

[32] S. Takabayashi, K. Okamoto, T. Nakatani, H. Sakaue, T. Takahagi; **Surface Analysis of Carbon–Hydrogen Bonds in Diamondlike Carbon Films by X-ray Photoelectron Spectroscopy**; Jpn. J. Appl. Phys. 48 (2009) p. 092304. doi: 10.1143/JJAP.48.092304

[33] D. Díaz-Fernández, E. Salas, J. Méndez, R.J.O. Mossanek, M. Abbate, C. Morales, G. Domínguez-Cañizares, G.R. Castro, A. Gutiérrez, L. Soriano; **Ultra-thin CoO films**

**grown on different oxide substrates: Size and support effects and chemical stability**; Journal of Alloys and Compounds; 758 (2018) pp. 5-13 doi:10.1016/j.jallcom.2018.05.112

[34] J. van Elp, J. L. Wieland, H. Eskes, P. Kuiper, G. A. Sawatzky, F. M. F. de Groot, T. S. Turner; **Electronic structure of CoO, Li-doped CoO, and $LiCoO_2$**; Phys. Rev. B 44 (1991) pp. 6090-6103. doi: 10.1103/PhysRevB.44.6090

[35] C.-H. Ho, C.-P. Tsai, C.-C. Chung, C.-Y. Tsai, F.-R. Chen, H.-J. Lin, C.-H. Lai; **Shape-Controlled Growth and Shape-Dependent Cation Site Occupancy of Monodisperse $Fe_3O_4$ Nanoparticles**; Chem. Mater.; 23 (2011) pp. 1753–1760. doi: 10.1021/cm102758u

[36] J. Park, K. An, Y. Hwang, J.-G Park, H.-J. Noh, J.-Y. Kim, J. -H. Park, N.-M. Hwang, T. Hyeon; **Ultra-large-scale syntheses of monodisperse nanocrystals**; Nat. Mater.; 3 (2004) pp. 891-895. doi: 10.1038/nmat1251

[37] S.A. Chambers, S.A. Joyce; **Surface termination, composition and reconstruction of $Fe_3O_4$ (001) and $\gamma$-$Fe_2O_3$ (001)**; Surf. Sci., 420 (1999) pp. 111-122. doi: 10.1016/S0039-6028(98)00657-8

[38] S. C. Petitto, E. M. Marsh, G. A. Carson, M. A. Langell; **Cobalt oxide surface chemistry: The interaction of CoO(100), $Co_3O_4$ (110), and $Co_3O_4$ (111) with oxygen and water**; J Mol. Catal. A-Chem; 281 (1–2) (2008) pp. 49-58; doi 10.1016/j.molcata.2007.08.023

[39] J.-C. Dupin, D. Gonbeau, P. Vinatier, A. Levasseur**; Systematic XPS studies of metal oxides, hydroxides and peroxides**; Phys. Chem. Chem. Phys.; 2 (2000) pp. 1319-1324; doi: 10.1039/a908800h

[40] A. Ganguly, S. Sharma, P. Papakonstantinou, J. Hamilton; **Probing the Thermal Deoxygenation of Graphene Oxide Using High-Resolution In Situ X-ray-Based Spectroscopies**; J. Phys. Chem. C; 115 (2011) pp. 17009–17019. doi: 10.1021/jp203741y

[41] C. Hontoria-Lucas, A.J. López-Peinado, J.D. López-González, M.L. Rojas-Cervantes, R.M. Martin-Aranda; **Study of oxygen-containing groups in a series of graphite oxides: physical and chemical characterization**; Carbon; 33 (1995) pp. 1585-1592. doi: 10.1016/0008-6223(95)00120-3

[42] R. Burgess, C. Buono, P. R. Davies, R. J. Davies, T. Legge, A. Lai, R. Lewis, D. J. Morgan, N. Robinson, D. J. Willock; **The functionalisation of graphite surfaces with nitric acid: Identification of functional groups and their effects on gold deposition**; J. Catal. 323 (2015) pp. 10-18. doi: 10.1016/j.jcat.2014.12.021

[43] B. Bowden, M. Davies, P. R. Davies, S. Guan, D. J. Morgan, V. Roberts, D. Wotton; **The deposition of metal nanoparticles on carbon surfaces: the role of specific functional groups**; Faraday Discuss. 208 (2018) pp. 455-47. doi: 10.1039/C7FD00210F

[44] O. Akhavan; **The effect of heat treatment on formation of graphene thin films from graphene oxide nanosheets**; Carbon; 48 (2010) pp. 509-519. doi: 10.1016/j.carbon.2009.09.069

[45] S. J. Sque, R. Jones, P. R. Briddon; **The transfer doping of graphite and graphene**; Phys. Stat. Sol.; 204 (2007) pp. 3078-3084; doi: 10.1002/pssa.200776313

[46] H. Hibino, H. Kageshima, M. Kotsugi, F. Maeda, F.-Z. Guo, Y. Watanabe; **Dependence of electronic properties of epitaxial few-layer graphene on the number of layers investigated by photoelectron emission microscopy**; Phys. Rev. B 79 (2009) 125437. doi: 10.1103/PhysRevB.79.125437

[47] X. Wang, Q. Peng, W. Zhu, G. Lei; **High performance of inverted polymer solar cells with cobalt oxide as hole-transporting layer**; Semicond. Sci. Technol.; 30 (2015) p. 055001. doi: 10.1088/0268-1242/30/5/055001

[48] D. Martínez-Martin, R. Longuinhos, J. G. Izquierdo, A. Marele, S. S. Alexandre, M. Jaafar, J. M. Gómez-Rodríguez, L. Bañares, J. M. Soler, J. Gómez-Herrero; **Atmospheric contaminants on graphitic surfaces**; Carbon 61 (2013) pp. 33-39. doi: 10.1016/j.carbon.2013.04.056

[49] G.C. McGonigal, R.H. Bernhardt, D.J. Thomson; **Imaging alkane layers at the liquid/graphite interface with the scanning tunneling microscope**; Appl. Phys. Lett. 57 (1990) pp. 28-30. doi: 10.1063/1.104234

[50] D. S. Wastl, F. Speck, E. Wutscher, M. Ostler, T. Seyller, Franz J. Giessibl; **Observation of 4 nm pitch stripe domains formed by exposing graphene to ambient air**; ACS Nano 7 (2013) pp. 10032–10037. doi: 10.1021/nn403988y

**Figure Captions**

Figure 1: a) C 1s NAP-XPS measurements of 2 ML CoO/HOPG sample exposed to different $O_2$ pressures during 1 hour. The spectra taken for each pressure at different times during this exposure are labeled accordingly. The inset shows a zoom of the temporal evolution of the samples exposed to $10^{-3}$ and $10^{-1}$ mbar, respectively; b) C 1s NAP-XPS measurements with three different photon energies at 1 mbar of $O_2$. Figure 1.a taken from [14].

Figure 2: Co 2p NAP-XPS measurements as a function of time of 2 ML CoO/HOPG heated to 415°C at UHV conditions; b) Co $L_{2,3}$ edge XAS measurements of 2 ML CoO/HOPG sample after reduction at 415ºC in UHV conditions at two beam polarizations: 0 and $\pi/2$. c) C 1s XPS measurement of clean and reduced HOPG.

Figure 3: Co 2p NAP-XPS measurements as a function of $O_2$ pressure and time of 2 ML CoO/HOPG at 415°C

Figure 4: a) C 1s NAP-XPS measurements as a function of $O_2$ pressure of 2 ML CoO/HOPG at 415°C; b) C 1s NAP-XPS measurements with three different photon energies for 1mbar of $O_2$ at 415°C; c) O 1s NAP-XPS measurements as a function of $O_2$ pressure of 2 ML CoO/HOPG at 415°C. Bottom: as grown CoO layer.

Figure 5: Top image: scheme of the experiment performed. Step 1: exposure to $O_2$ of the as grown deposit; step 2 re-oxidation process consisting of two stages: reduction at 400°C under UHV conditions and introduction of $O_2$ at that same temperature. For each of these three stages AFM (top) and Raman images of the D/G band ratio (bottom). The red squares in the AFM images are the zones mapped with Raman spectroscopy at their respective bottom images. In the case that there is not a red square, it means that the whole image has been mapped. All Raman images have been normalized to the same units for comparison purposes.

Figure 6: Basic scheme of the carbon gasification reaction induced by cobalt oxide nanoparticles on graphite via re-oxidation process.

Figure 7: a) and b) topography and phase images, respectively, of 2 ML CoO/HOPG after re-oxidation process. $CoO_x$ clusters and nano-rings are shown; c) detail of nano-rings and nano-strips in topography image; d) phase image of $CoO_x$ clusters along graphite steps and terraces surrounded by nanorings. e) topography detail of nanorings and nanostrips

with their corresponding profiles. Images taken with Nanotec AFM microscope at room conditions.

Figure 8: a) AFM topography image and b) work function map of 2 ML CoO/HOPG after re-oxidation process. A Cypher VRS microscope was used at RT and $N_2$ atmosphere.